IEEE Robotics and Automation Letters (RA-L) paper, presented at ICRA 2026, Vienna, Austria. Cite as RA-L paper.

Steering Performance Optimization for Wheeled Mobile Robots in Granular Media via DRFM: Enhancing Locomotion Precision and Energy Efficiency

Chuang Cao[1], Lei Huang[1], Feiyu Zhang[1], and Yuehong Yin[1,*], Member, IEEE

***Abstract*—Degraded steering performance and increased energy consumption present significant barriers to deploying wheeled mobile robots (WMRs) in granular media such as sand and lunar regolith. This study presents and experimentally validates a systematic optimization framework based on the Dynamic Resistive Force Model (DRFM). By integrating the DRFM with a four-wheel vehicle dynamics model featuring front-wheel steering, this approach effectively captures wheel–terrain interactions in granular materials. Subject to a prescribed trajectory root-mean-square error constraint, the framework minimizes energy consumption per unit distance while determining optimal front-wheel steering angles and wheel-speed ratios. Experiments demonstrate that the active steering strategy reduces energy consumption per unit distance by 12.3% while maintaining an average normalized trajectory root-mean-square error of 6.5% across the tested turning radii. The proposed method is demonstrably effective for our rover equipped with wheel geometries that depart markedly from conventional shapes, suggesting its potential to generalize to arbitrary wheel geometries.**

***Index Terms*—Wheeled robots, granular media, steering optimization, dynamic system modeling**

I. Introduction

In the ever-expanding field of robotics, wheeled mobile robots (WMRs) have emerged as versatile platforms for a wide range of applications, from exploration in hazardous environments such as disaster-stricken areas and extraterrestrial surfaces to industrial material handling and agricultural operations [1]–[3]. However, when operating in granular media, which include substances like sand, gravel, or powder, WMRs face significant challenges that severely impact steering performance, thereby compromising both locomotion precision and efficiency [4].

Granular media possess complex mechanical properties, and the interaction between wheels and granular particles is highly non-linear [5], [6]. As the wheels rotate and exert forces on the granular material, the particles rearrange themselves in a way that can lead to unpredictable sinkage, slip, and interaction forces [7], [8]. These phenomena can cause the robot to deviate from its intended path, reducing its locomotion precision. For example, in an extraterrestrial exploration scenario where the surface is covered with regolith (a form of granular media), a slight deviation in steering due to wheel-soil interaction can misdirect the rover and potentially cause it to encounter obstacles or miss scientific targets [2]. Inefficient locomotion in granular media also results in increased energy consumption [9]. The energy wasted in overcoming the resistance caused by improper steering and excessive slip not only limits the operational range of the WMR but also requires larger and heavier power sources, further complicating the design and deployment of these robots.

Conventionally, the motion control of WMRs often relies on the concept of non-holonomic constraints. These constraints assume a certain relationship between the linear and angular velocities of the wheels, which simplifies the motion planning and control algorithms in typical flat-terrain or rigid-surface scenarios [10], [11]. However, in granular media, non-holonomic constraints prove to be inapplicable. The unpredictable nature of granular media gives rise to slip and skid of the wheels, and the forces exerted by the granular particles on the wheels vary instantaneously. As a result, the relationships that non-holonomic constraints are built upon break down completely [12]. For instance, the classic Ackermann steering model, which is based on non-holonomic constraints, cannot accurately predict or control the motion of a WMR in sand dunes. Here, wheel sinkage can occur, and lateral slip might change direction, rendering the model ineffective [13]. To address the aforementioned challenges, it is essential to model the dynamics of WMRs operating in granular media.

Some studies rely on sensor-based feedback. For instance, inertial measurement units (IMUs) and wheel encoders can provide information about the robot's orientation and wheel rotation, and these data are then used to correct the steering [14], [15]. Nevertheless, these sensors have limitations. IMUs may be affected by vibrations in the granular environment, leading to inaccurate orientation estimates. Wheel encoders, on the other hand, can only measure wheel rotation and do not directly account for the slip that occurs between

Manuscript received: July 10, 2025; Revised: September 30, 2025; Accepted: October 25, 2025.

This paper was recommended for publication by Editor Soon-Jo Chung upon evaluation of the Associate Editor and Reviewers' comments.

The authors are with the State Key Laboratory of Mechanical System and Vibration, Institute of Robotics, Shanghai Jiao Tong University, Shanghai 200240, China (e-mail: caochuang@sjtu.edu.cn; hl_18sjtu@sjtu.edu.cn; zhangfy0659@sjtu.edu.cn; yhyin@sjtu.edu.cn).

Chuang Cao and Lei Huang contributed equally to this work.

Digital Object Identifier (DOI): see top of this page.

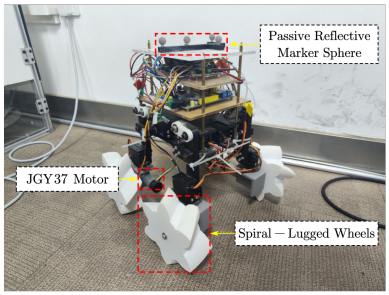

Fig. 1. Custom-built four-wheeled mobile robot experimental platform with a spiral-lugged wheel. This platform is used to validate the effectiveness of DRFM-based modeling and steering optimization strategies in physical sandbox experiments.

the wheels and the granular media, which is a major contributor to steering inaccuracies [16].

Another approach is to use the force exerted by particulate media on the wheel as input to analyze the WMR dynamics [17], [18]. However, accurately predicting the forces exerted by granular media on the wheels is extremely difficult [11]. Granular particles' behavior is influenced by numerous factors such as particle friction, packing density, and the dynamic state of the robot [19], [20]. These forces can change drastically even with minor variations in the robot's locomotion or the local terrain characteristics within the granular media [21], [22]. The inability to predict these forces precisely means that traditional control strategies, which rely on pre-defined force-locomotion relationships, fail to adapt to the actual operating conditions.

To address these limitations, this letter adopts the Dynamic Resistive Force Model (DRFM) proposed in [23] as the wheel–terrain interaction model for locomotion analysis on granular terrain. The main contributions of this work are twofold. First, we establish a DRFM-based rigid-body dynamic model for a four-wheeled mobile robot, enabling the prediction of its acceleration, velocity, and trajectory on granular terrain. Second, we develop a steering-parameter optimization framework that uses trajectory root-mean-square error as an accuracy constraint and minimizes energy consumption per unit distance through a Sobol sequence-based parameter sweep. The resulting steering strategies are further validated through physical sandbox experiments. An overview of the experimental platform used throughout this study is shown in Fig. 1.

The remainder of this letter is organized as follows: Section II develops a DRFM-based dynamic model that captures the coupled wheel–terrain interactions of a four-wheeled mobile robot operating in granular media. Section III formulates the steering-parameter optimization problem and details a Sobol sequence-based parameter sweep for constrained single-objective steering optimization under a trajectory-accuracy requirement. Section IV describes the sandbox experimental setup and reports physical trials that benchmark the optimized steering strategy against a differential-steering baseline. Finally, Section V concludes the letter and outlines directions for extending the DRFM framework to more complex terrains and real-time control applications.

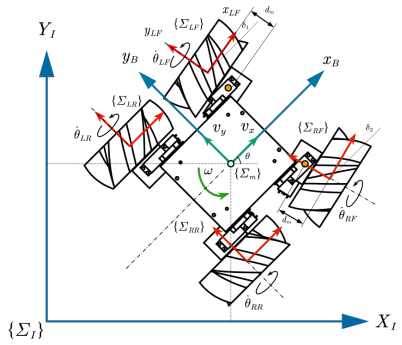

Fig. 2. Schematic representation of the WMR structure and coordinate systems.

II. Dynamic System Modeling

We first develop a dynamic model to predict and optimize WMR steering in granular media. It starts from the robot structure and coordinate systems and uses the Dynamic Resistive Force Method (DRFM) to capture wheel-terrain interaction.

A. Robot Structure and Coordinate Systems

The WMR uses a four-wheel architecture designed for mobility in challenging terrains (Fig. 2).

- Wheels: The robot has four spiral-lugged wheels. Their geometry, optimized in prior work [23], enhances performance in loose granular substrates. For practical reasons, we supplement the original single-sided spiral blade with an axially mirrored blade on the opposite side, enabling efficient forward and backward motion in granular media.
- Configuration: The front wheels (1: FL, 2: FR) are independently steerable about vertical pivots; the rear wheels (3: RL, 4: RR) are fixed relative to the chassis.

To describe the robot's motion and forces, we define the following coordinate systems (Fig. 2):

1) **Inertial Frame ($\mathcal{I}$):** A fixed global frame $\{X, Y, Z\}_{\mathcal{I}}$ with the Z-axis upwards. Robot position and orientation are expressed in this frame. The robot heading (yaw) is denoted by θ.
2) **Body Frame ($\mathcal{B}$):** A body frame $\{x, y, z\}_{\mathcal{B}}$ attached at the robot's center of mass (CoM). Forces and torques are resolved in this frame. We denote the body-frame planar velocities by v_x (forward along $x_{\mathcal{B}}$) and v_y (lateral along $y_{\mathcal{B}}$), and the yaw rate by ω about $z_{\mathcal{B}}$ (i.e., $\dot{\theta}$).
3) **Wheel Frames ($\mathcal{W}_i$):** For each wheel i, $\{x_w, y_w, z_w\}_{\mathcal{W}_i}$ is centered at the axle. The x_w-axis aligns with the travel direction set by the steering angle; y_w is the rotation axis; z_w completes a right-handed frame. The front wheels have an axle-pivot offset d_m. The front-wheel steering angles are denoted by δ_i. Wheel-terrain forces from DRFM are expressed in these frames.

B. Dynamic Resistive Force Method (DRFM)

We adopt DRFM [23] to compute wheel-terrain interaction forces under dynamic motion.

Given the wheel-driven locomotion, each wheel's linear and angular velocities are known at every time step. For a surface element at local position r, the local velocity is:

$$v = v_l + v_a \times r \tag{1}$$

In this equation, v_l denotes the linear velocity of the wheel, v_a represents the angular velocity, and r is the position vector of the surface element relative to the wheel center. The element pose is described by unit vectors $\hat{e}_1$ (surface normal), $\hat{e}_3$ (upward), and $\hat{e}_2 = \hat{e}_1 \times \hat{e}_3$. DRFM couples drag and lift in the e_2-e_3 plane by projecting $\mathbf{v}$ onto this plane to obtain the unit direction $\hat{e}_{23}$ for the in-plane force model.

According to [23], the resistive force on each element is:

$$F_e = f_1(\hat{v}, \hat{e}_1)\hat{F}_1 + f_2(\hat{v}, \hat{e}_{23})\hat{F}_{23} + F_v \tag{2}$$

where $\hat{F}_1$ and $\hat{F}_{23}$ are resultant directions associated with the element normal $\hat{e}_1$ and the in-plane e_2–e_3 directions. In the e_2–e_3 plane, the in-plane resultant $\hat{F}_{23}$ is driven by the tangential velocity component v_{23} (yield stress plus flow resistance), while along e_1 the normal resultant $\hat{F}_1$ is driven by the normal component v_1 (mainly flow resistance), where v_1 and v_{23} are the components of the velocity v along the e_1 and e_2–e_3 directions. Further details were well explained in our previous work [23].

The dynamic term F_v accounts for momentum exchange with the medium and scales with $\rho_c v^2$ via coefficient λ, where ρ_c denotes the granular medium density. This term acts opposite to $\hat{v}$ and is integrated over the area normal to $\mathbf{v}$ [23]:

$$F_v = \int \left[-\lambda \rho_c v^2\right] \hat{v}\, ds_\perp \tag{3}$$

The total resistive force F acting on the body is obtained by integrating local force contributions over the entire contact surface S:

$$F = \int_S F_e ds \tag{4}$$

For simulation, the wheel surface is discretized into N triangular patches (Fig. 3):

$$\mathbf{F}_i^{\mathcal{W}_i} = \sum_{j=1}^{N} d\mathbf{F}_j \tag{5}$$

where $d\mathbf{F}_j$ is the resistive force exerted on the j-th surface element by the granular medium. The total force $\mathbf{F}_i^{\mathcal{W}_i}$ acting on the i-th wheel is the sum of these elemental contributions.

In general, DRFM extends the terradynamics framework of [5], which demonstrated that resistive stresses on two-dimensional (2-D) intruders in granular media share common structure, to three-dimensional (3-D) intruders and incorporates dynamic effects, enabling a unified force model that can be ported across substrates by re-calibrating a small set of coefficients. In this research, we adhere to the standard DRFM workflow used in prior literature. Readers are referred to [23] for complete derivations of Eqs. (1)–(4) and the parameter-identification procedure. We calibrate both the quasi-static and dynamic coefficients for the target medium—in our case, dry quartz sand—following the protocol of [23].

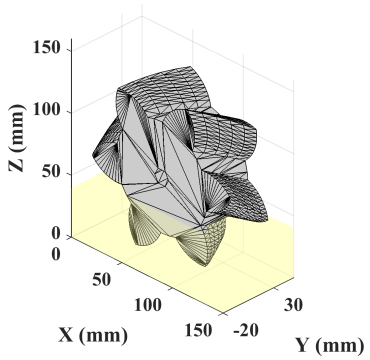

Fig. 3. Triangular mesh discretization of the wheel surface for DRFM application. The light yellow region represents the granular medium, where the immersed portion of the wheel experiences resistive forces during motion.

C. Force and Torque Synthesis

Once the wheel-terrain interaction forces $\mathbf{F}_i^{\mathcal{W}_i}$ for each wheel i are known, they are transformed to the robot's body frame $\mathcal{B}$ and synthesized to determine the net external influences.

The net force $\mathbf{F}_{\text{net}}^{\mathcal{B}}$ acting on the WMR in the body frame $\mathcal{B}$ is given by the sum of the transformed forces from all four wheels and the gravitational force:

$$\mathbf{F}_{\text{net}}^{\mathcal{B}} = \sum_{i=1}^{4} R_{\mathcal{W}_i \to \mathcal{B}} \mathbf{F}_i^{\mathcal{W}_i} + m\, \mathbf{g}^{\mathcal{B}}, \tag{6}$$

where m is the total mass of the robot, and $\mathbf{g}^{\mathcal{B}} = [0, 0, -g]^{\mathsf{T}}$ is the gravitational acceleration vector expressed in the body frame $\mathcal{B}$. The matrix $R_{\mathcal{W}_i \to \mathcal{B}}$ is the rotation matrix that transforms vectors from the i-th wheel frame $\mathcal{W}_i$ to the body frame $\mathcal{B}$. This transformation depends on the steering angle δ_i of the respective front wheel (for $i = 1, 2$) and its fixed mounting orientation relative to the chassis. Because the sinkage changes dynamically during motion, the vertical degree of freedom is integrated rather than constrained. The vertical acceleration of the CoM in the body frame follows directly from Eq. (6):

$$a_z^{\mathcal{B}} = \frac{\left(\mathbf{F}_{\text{net}}^{\mathcal{B}}\right)_z}{m}, \tag{7}$$

and the vertical position z (i.e., the sinkage) is updated at each time step through the semi-implicit Euler integration (Eq. (14)), in the same manner as x and y. Before the simulation, we measure the static sinkage of each wheel of the real robot at rest to establish the initial condition z_0 with $\dot{z}_0 = 0$. The local element depth used in DRFM then follows from this evolving sinkage. The granular medium influences sinkage only through the DRFM parameters.

For analyzing the robot's steering behavior, the net yaw torque τ_z about the z-axis of the body frame $\mathcal{B}$ (passing through the CoM) is crucial. It is computed as the

z-component of the sum of moments generated by each transformed wheel force:

$$\tau_z = \left[\sum_{i=1}^{4} \mathbf{r}_i^{\mathcal{B}} \times \left(R_{\mathcal{W}_i \to \mathcal{B}} \mathbf{F}_i^{\mathcal{W}_i} \right) \right]_z, \tag{8}$$

where $\mathbf{r}_i^{\mathcal{B}} = [x_i, y_i, z_i]^\mathsf{T}$ represents the position vector from the robot's CoM to the i-th wheel force application point in the body frame $\mathcal{B}$. For the front wheels, z_i includes the axle-pivot offset d_m.

These resultant forces and torques are subsequently used as inputs to the equations of motion (Section II-D) to determine the robot's translational and rotational accelerations.

D. Semi-Implicit Euler Integration

The equations of motion, derived from the net forces and torques computed in Section II-C, are integrated numerically to simulate the robot's trajectory over time. This study employs a semi-implicit Euler integration method, chosen for its computational efficiency which aligns with the requirement for rapid simulations in the extensive parameter sweeps.

The state of the WMR is defined by its position and heading angle in the inertial frame $\mathcal{I}$. The state vector $\mathbf{X}$ is given by:

$$\mathbf{X} = [x, y, z, \theta]^\mathsf{T}, \tag{9}$$

where (x, y, z) are the Cartesian coordinates of the robot's CoM, and θ is its yaw angle. The vertical coordinate z is integrated from the vertical dynamics (Eq. (7)), with its initial value z_0 set by the measured static sinkage.

The first time derivative of the state vector, $\dot{\mathbf{X}}$, represents the robot's inertial velocities:

$$\dot{\mathbf{X}} = [\dot{x}, \dot{y}, \dot{z}, \omega]^\mathsf{T}, \tag{10}$$

where $(\dot{x}, \dot{y}, \dot{z})$ are the linear velocity components of the CoM in $\mathcal{I}$, and $\omega = \dot{\theta}$ is its yaw rate.

The linear acceleration of the robot's CoM, expressed in the body frame $\mathcal{B}$, is obtained from Eq. (6):

$$\mathbf{a}^{\mathcal{B}} = [a_x^{\mathcal{B}}, a_y^{\mathcal{B}}, a_z^{\mathcal{B}}]^\mathsf{T} = \frac{\mathbf{F}_{\text{net}}^{\mathcal{B}}}{m}. \tag{11}$$

The yaw angular acceleration $\dot{\omega}$ is determined by the net yaw torque τ_z from Eq. (8) and the robot's moment of inertia I_{zz} about the z-axis of its body frame:

$$\dot{\omega} = \frac{\tau_z}{I_{zz}}. \tag{12}$$

To update the inertial velocities $\dot{\mathbf{X}}$, the body-frame linear accelerations $\mathbf{a}^{\mathcal{B}}$ evaluated at time t_n are first transformed into the inertial frame $\mathcal{I}$ using the robot orientation θ_{n-1} (via the rotation matrix $R_{\mathcal{B}\to\mathcal{I}}(\theta_{n-1})$). Let this transformed linear acceleration be $\mathbf{a}^{\mathcal{I}}(t_n)$. The vector of generalized accelerations for the n-th time step is then:

$$\ddot{\mathbf{X}}_n = [(a_x^{\mathcal{I}})_n, (a_y^{\mathcal{I}})_n, (a_z^{\mathcal{I}})_n, \dot{\omega}_n]^\mathsf{T}. \tag{13}$$

The state is updated at discrete time steps. Given the state $\mathbf{X}_{n-1}$ and velocities $\dot{\mathbf{X}}_{n-1}$ at time t_{n-1}, the semi-implicit Euler update to time $t_n = t_{n-1} + \Delta t$ is written as:

$$\begin{cases} \dot{\mathbf{X}}_n = \dot{\mathbf{X}}_{n-1} + \ddot{\mathbf{X}}_n \cdot \Delta t \\ \mathbf{X}_n = \mathbf{X}_{n-1} + \dot{\mathbf{X}}_n \cdot \Delta t \end{cases} \tag{14}$$

The time step Δt is chosen to balance simulation efficiency and stability.

E. Simulation Performance Validation

The simulation is implemented in Python (leveraging Numba for acceleration) with multi-core parallelism and streamlined memory flow. A $30\,\text{s}$ simulation with $\Delta t = 2\,\text{ms}$ (15,000 steps) completes in $21\,\text{s}$ on an Intel Core i7–12700 (real-time factor ≈ 1.43), i.e., $\sim 1.4\,\text{ms}$ per step ($\sim 714\,\text{Hz}$). This leaves substantial headroom for real-time control at 350–500 Hz when reserving 30–50% of the cycle for I/O and scheduling.

F. Wheel Force Distribution Analysis

Before discussing the force characteristics, Fig. 4 illustrates the time histories of the wheel-terrain interaction forces along the x, y, and z axes for all four wheels.

A number of salient features can be extracted from these curves:

- F_x: Front wheels oppose the rears, producing a differential moment that drives yaw.
- F_y: Lateral forces on the fronts largely balance those on the rears, keeping net side thrust near zero; a residual front component aids the yaw moment.
- F_z: Vertical loads are dominated by gravity and stabilize after transients, with larger loads on the rear due to the CoM location.

These observations confirm that the proposed dynamic model provides numerically stable force predictions suitable for subsequent optimization or control design tasks.

III. Steering Optimization

Building on the dynamic model developed in Section II, this section presents a methodology for optimizing the steering performance of the WMR in granular media. The core idea is to leverage the model's computational efficiency to perform a large-scale parameter sweep, identifying control parameter sets that satisfy the trajectory-accuracy requirement while reducing energy consumption.

A. Optimization Objective

The steering optimization aims to identify a set of control parameters, $\boldsymbol{\alpha}$ (defined in Section III-B), that enables the WMR to follow a predefined circular arc trajectory while minimizing energy expenditure. This problem is formulated as a constrained single-objective optimization problem, in which the energy consumption per unit distance is minimized subject to a trajectory-tracking accuracy constraint. Two performance metrics are used to evaluate each candidate parameter set:

1) **Trajectory Tracking Accuracy (ε_{RMS}):** This metric quantifies how closely the robot follows the desired circular arc trajectory and is used as an accuracy constraint.
2) **Energy Efficiency per Distance (E_{dist}):** This metric quantifies the energy consumed per unit distance traveled and is used as the optimization objective.

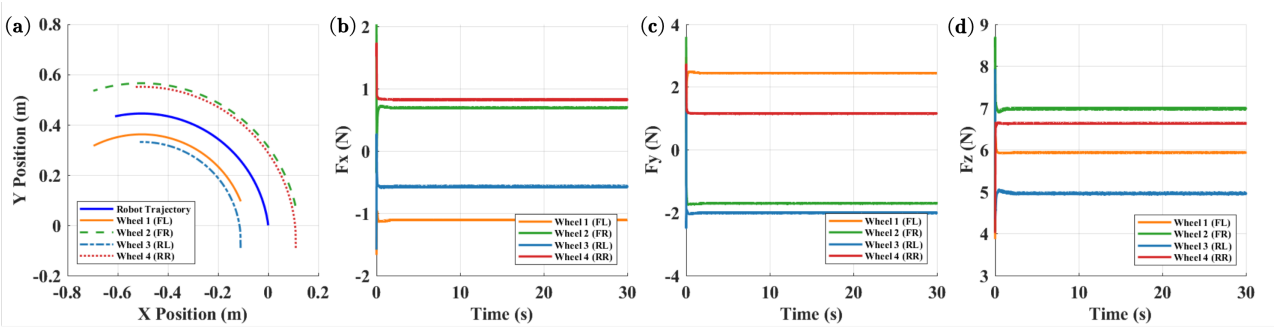

Fig. 4. Simulated wheel forces along x, y, and z axes and the robot CoM trajectory over a 30-s left turn. Colors denote wheels 1-4 (FL, FR, RL, RR); the blue trace is the CoM path.

TABLE I
CONTROL PARAMETERS DEFINITION

Parameter	Control Variable	Range	Formula
α_1	FL Steering Angle	$[0°, 15°]$	$\delta_{\text{FL}} = \alpha_1$
α_2	FR Steering Angle	$[0°, 15°]$	$\delta_{\text{FR}} = \alpha_2$
α_3	FR Velocity Ratio	$[0, 1.5]$	$\omega_{\text{FR}} = \alpha_3\omega_{\text{ref}}$
α_4	RL Velocity Ratio	$[0, 1.5]$	$\omega_{\text{RL}} = \alpha_4\omega_{\text{ref}}$
α_5	RR Velocity Ratio	$[0, 1.5]$	$\omega_{\text{RR}} = \alpha_5\omega_{\text{ref}}$

The optimization is carried out in a constrained single-objective manner. For each candidate parameter set $\boldsymbol{\alpha}$, the trajectory RMS error $\varepsilon_{\text{RMS}}(\boldsymbol{\alpha})$ is first evaluated against an allowable threshold ε_{acc}. Only parameter sets satisfying $\varepsilon_{\text{RMS}}(\boldsymbol{\alpha}) \leq \varepsilon_{\text{acc}}$ are retained. Among these feasible solutions, the strategy with the lowest energy consumption per unit distance, $E_{\text{dist}}(\boldsymbol{\alpha})$, is selected as the optimal result.

B. Optimization Variable Parameter Space

To comprehensively explore potential steering strategies, we define a set of control parameters, $\boldsymbol{\alpha}$, that govern the front wheel absolute steering angles and the relative angular velocities of the four wheels. This parameterization allows for flexible, decoupled control inputs beyond traditional coupled steering models. The vector of five optimization variables is $\boldsymbol{\alpha} = \{\alpha_1, \alpha_2, \alpha_3, \alpha_4, \alpha_5\}$.

The mapping between these parameters and the corresponding physical control inputs is summarized in Table I. The parameter ranges are defined as follows: $\alpha_1, \alpha_2 \in [0°, 15°]$ (maximum steering angle to avoid mechanical interference), and $\alpha_3, \alpha_4, \alpha_5 \in [0, 1.5]$. The parameter $\omega_{\text{FL,ref}}$ represents a reference angular velocity for the front-left wheel, which is set based on the desired nominal forward speed for a given trajectory tracking task. In the velocity ratio formulas, $\omega_{\text{ref}} = \omega_{\text{FL,ref}}$ serves as the reference angular velocity for normalizing the wheel speeds.

C. Optimization Method

The parameter space is sampled using Sobol sequences, which are quasi-random low-discrepancy sequences. We generate $N = 8,000$ parameter vectors from the 5-dimensional parameter space using Sobol sequences. The core of our optimization approach lies in leveraging the computational speed of the DRFM-based dynamic model (Section II) to perform a large-scale, direct evaluation of steering strategies. Unlike iterative optimization algorithms that sequentially search for an optimum, our method explores the parameter space in a massively parallel fashion.

1) Sobol Sequence-Based Parameter Sweep: The complete parameter-sweep routine is summarized in Algorithm 1.

Algorithm 1 Sobol Sequence-Based Parameter Sweep

Require: N (number of samples); parameter ranges in Table I
Ensure: Dataset $\mathcal{D} = \{(\boldsymbol{\alpha}^{(k)}, \varepsilon_{\text{RMS}}^{(k)}, E_{\text{dist}}^{(k)})\}_{k=1}^{N}$
1: Generate N Sobol sequence samples $\mathbf{s}^{(k)} \in [0, 1]^5$
2: **for** $k \leftarrow 1$ **to** N **parallel do**
3: Map $\mathbf{s}^{(k)}$ to physical parameters $\boldsymbol{\alpha}^{(k)}$
4: Simulate the WMR following the reference arc using $\boldsymbol{\alpha}^{(k)}$
5: Compute $\varepsilon_{\text{RMS}}^{(k)}$ and $E_{\text{dist}}^{(k)}$
6: Store $(\boldsymbol{\alpha}^{(k)}, \varepsilon_{\text{RMS}}^{(k)}, E_{\text{dist}}^{(k)})$ in $\mathcal{D}$
7: **end for**

2) Circular Arc Trajectory Deviation Assessment: The optimization process relies on accurately quantifying the deviation between the robot's actual trajectory and the desired circular turning radius. This assessment is conducted through a systematic three-step procedure. Initially, a reference circular arc trajectory is constructed based on the desired turning radius R_{ref}. Subsequently, for each actual trajectory point, the Euclidean distance to its nearest sampled point on the reference arc is calculated. Finally, the RMS error is computed to provide a comprehensive measure of trajectory tracking accuracy.

The direct simulation approach employed in this study offers several distinct advantages over traditional optimization methods. Its global nature enables comprehensive exploration of the parameter space, significantly reducing the risk of converging to local optima through large-scale scanning. Furthermore, the independence of each parameter combination evaluation eliminates the need for gradient information, making the method robust and computationally efficient. Additionally, the inherent parallelism of this approach allows for full utilization of multi-core CPU architectures, substantially accelerating the computation process. Finally, the use of Sobol sequences ensures uniform coverage of the parameter space, providing systematic exploration without clustering or gaps in the search domain.

D. Evaluation Metrics

To quantitatively assess the performance of each steering strategy $\boldsymbol{\alpha}^{(k)}$, two evaluation metrics are computed from the simulation data, corresponding to the trajectory-accuracy constraint and the energy-efficiency objective defined in Section III-A.

1) **Trajectory RMS Error ($\varepsilon_{\mathrm{RMS}}$):** This metric quantifies the deviation of the robot's actual trajectory from the desired circular arc trajectory. For an actual trajectory represented by M sampled positions $\mathbf{p}_{\mathrm{act},j}$, let $\mathbf{p}_{\mathrm{arc},j}$ denote the nearest sampled point on the reference arc to $\mathbf{p}_{\mathrm{act},j}$. The $\varepsilon_{\mathrm{RMS}}$ is then calculated as:

$$\varepsilon_{\mathrm{RMS}} = \sqrt{\frac{1}{M}\sum_{j=1}^{M} \|\mathbf{p}_{\mathrm{act},j} - \mathbf{p}_{\mathrm{arc},j}\|^2}, \tag{15}$$

where $\|\cdot\|$ denotes the Euclidean norm. A lower $\varepsilon_{\mathrm{RMS}}$ indicates better tracking accuracy. For cross-radius comparison, we also report a normalized measure $\varepsilon_{\mathrm{RMS}}/R$ (expressed as a percentage) in the experimental results.

2) **Energy per Unit Distance (E_{dist}):** This metric evaluates the energy efficiency of the robot. It is defined as the total energy consumed by all wheel motors, E_{total}, divided by the total distance traveled along the actual trajectory, L_{traj}:

$$E_{\mathrm{dist}} = \frac{E_{\mathrm{total}}}{L_{\mathrm{traj}}}, \tag{16}$$

where E_{total} is computed by integrating the instantaneous power consumed by each motor over the simulation duration: $E_{\mathrm{total}} = \sum_{i=1}^{4} \int_0^{T_{sim}} P_i(t)dt$, where $P_i(t)$ is the power of motor i at time t, and T_{sim} is the total simulation time. A lower E_{dist} signifies better energy efficiency.

These two metrics, $\varepsilon_{\mathrm{RMS}}$ and E_{dist}, are calculated for each of the $N = 8,000$ simulated steering strategies, forming a performance dataset used in the subsequent filtering stage.

E. Two-Stage Filtering

Given the N pairs of $(\varepsilon_{\mathrm{RMS}}^{(k)}, E_{\mathrm{dist}}^{(k)})$ obtained from the parameter sweep, the subsequent decision logic is formalized in Algorithm 2. This procedure directly implements the constrained optimization framework introduced earlier: candidate strategies are first filtered according to the trajectory-accuracy requirement, and the remaining feasible solutions are then ranked by energy consumption per unit distance. $\varepsilon_{\mathrm{acc}}$ is assigned based on the allowable deviation (tolerance). While a smaller value generally yields a more accurate trajectory, it also narrows the set of steering strategies available for energy-efficiency optimization.

Algorithm 2 Two-Stage Filtering of Simulation Results

Require: Dataset $\mathcal{D}$; accuracy threshold $\varepsilon_{\mathrm{acc}}$
Ensure: Optimal set $\mathcal{S}_{\mathrm{opt}}$
1: $\mathcal{S}_{\mathrm{acc}} \leftarrow \{\boldsymbol{\alpha}^{(k)} \mid \varepsilon_{\mathrm{RMS}}^{(k)} \le \varepsilon_{\mathrm{acc}}\}$ ▷ Accuracy filter
2: Sort $\mathcal{S}_{\mathrm{acc}}$ by ascending $E_{\mathrm{dist}}^{(k)}$
3: $\mathcal{S}_{\mathrm{opt}} \leftarrow$ top-ranked element(s) in $\mathcal{S}_{\mathrm{acc}}$

IV. Physical Experiment Validation

To validate the effectiveness of the steering control strategies optimized in simulation, this study constructed a dedicated granular media experimental platform. The physical experiments aim to demonstrate the practical applicability of the optimized strategies by comparing trajectory accuracy and energy efficiency under controlled conditions.

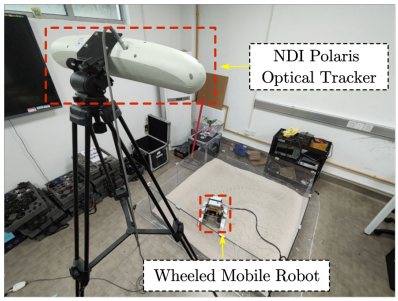

Fig. 5. Overall experimental platform layout, including 1.5m×1.5m sandbox, Ackermann-like four-wheel robot, and IR positioning system.

A. Experimental Platform and Testing Environment

The experimental platform consists of a closed sandbox testbed, a mobile robot platform, and a data acquisition system. Fig. 5 illustrates the overall experimental platform layout.

1) Experimental Environment: The experimental field employs a PC board fence to construct a $1.5\,\mathrm{m} \times 1.5\,\mathrm{m}$ closed rectangular sandbox filled with quartz sand as the granular medium. The sand has an average particle size of 0.5-0.8 mm and a bulk density of approximately $1650\,\mathrm{kg/m^3}$. The fill depth is maintained at $0.15\,\mathrm{m}$ to provide sufficient thickness for vehicle operation. The surface is raked and leveled before each test group to ensure initial condition consistency across all trials.

2) Robot Platform: The experiment employs a custom Ackermann-like four-wheel mobile robot, the same one used in the simulation model. The chassis dimensions are $0.30\,\mathrm{m} \times 0.20\,\mathrm{m} \times 0.15\,\mathrm{m}$ (Length × Width × Height) with a total mass of $3\,\mathrm{kg}$. The vehicle features four identical spiral-lugged wheels with a diameter of $0.12\,\mathrm{m}$ and a width of $0.06\,\mathrm{m}$. The drive system uses an STM32 microcontroller, front-wheel servo steering with a range of $\pm 15°$, and four independent DC motor drives powered by a regulated $12\,\mathrm{V}$ supply.

3) Measurement System: The measurement system integrates multiple sensors for comprehensive data collection. Pose measurement is achieved through an IR-based visual positioning system with reflective markers mounted on top of the robot, providing position accuracy of $\pm 0.1\,\mathrm{mm}$ at $100\,\mathrm{Hz}$ sampling frequency. Current measurement utilizes a digital current recorder with $1000\,\mathrm{Hz}$ sampling frequency and measurement accuracy of $\pm 0.01\,\mathrm{A}$. All sensor data are synchronized through timestamps to ensure temporal correspondence between trajectory and energy consumption data.

TABLE II
EXPERIMENTAL CONFIGURATION AND OPTIMIZED CONTROL PARAMETERS

No.	Radius (m)	Steering Angles $(^\circ)$ {FL, FR}	Angular Velocities (RPM) {FL, FR, RL, RR}
G1	0.45	{7, 12}	{6.0, 7.2, 5.4, 7.2}
G2	0.45	{0, 0}	{6.0, 7.8, 4.8, 7.2}
G3	0.60	{7, 12}	{6.0, 7.2, 4.8, 7.2}
G4	0.60	{0, 0}	{6.0, 7.2, 3.6, 6.6}
G5	0.90	{4, 13}	{6.0, 6.0, 3.6, 7.2}
G6	0.90	{0, 0}	{6.0, 7.2, 3.0, 6.6}

B. Task Definition

The experimental task is designed as circular arc tracking with 90° sector trajectories at three different turning radii: $R \in \{0.45, 0.60, 0.90\}\,\mathrm{m}$. The robot's initial position is uniformly set at the arc starting point with initial orientation along the arc tangent direction. Motion control is based on a reference angular velocity of $6\,\mathrm{RPM}$ for the front-left wheel, while the remaining three wheel angular velocities are determined by proportional relationships derived from optimization parameters.

This study employs two key metrics to evaluate steering performance: the trajectory RMS error $\varepsilon_{\mathrm{RMS}}$ for tracking accuracy and the energy consumption per unit distance E_{dist} for energy efficiency. The latter is computed as:

$$E_{\mathrm{dist}} = \frac{1}{D}\int_0^T I(t)\cdot V\,dt \tag{17}$$

where $V = 12\,\mathrm{V}$ is the supply voltage, $I(t)$ is the total current sampled at $1000\,\mathrm{Hz}$, and D is the actual travel distance. Energy consumption is expressed in $\mathrm{J/m}$ units.

C. Experimental Configurations

Based on the DRFM-based simulation optimization results presented in the previous sections, the physical experiments use the optimized control parameters for validation under different turning radii. The control inputs consist of the front-wheel steering angles and the angular velocity ratios of all four wheels relative to the front-left wheel. Table II lists the final parameter sets used in all experimental trials.

1) Optimized Control Parameters: All control parameters listed in Table II are taken from the two-stage filtering optimization procedure based on 8,000 simulations, and each set corresponds to the minimum-energy feasible solution under the trajectory-accuracy constraint for the specified turning radius. In the table notation, FL, FR, RL, and RR denote the Front Left, Front Right, Rear Left, and Rear Right wheels, respectively. The FL wheel angular velocity is fixed at 6.0 RPM as the reference, and the speeds of the other wheels are prescribed as proportional ratios. Odd-numbered groups (G1, G3, G5) correspond to the front-steering (FS) strategy, whereas even-numbered groups (G2, G4, G6) correspond to the differential-steering (DS) strategy.

2) Experimental Execution: Each experimental group was repeated five times to ensure statistical reliability. The preset control parameters were kept constant throughout each run, with no online adjustment during execution. The supplementary video provides representative demonstrations of the physical experiments.

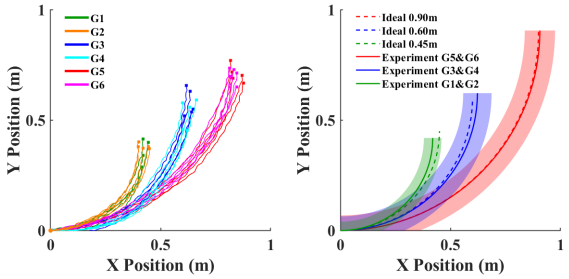

Fig. 6. Consolidated experimental results. Left: recorded trajectories for all six experimental groups at three turning radii. Right: time histories of the trajectory error with shaded $\pm 1\sigma$ envelopes; the solid line indicates the mean radius computed from trajectories of the combined groups. FS: Front Steering; DS: Differential Steering.

TABLE III
RMS TRAJECTORY ERROR RELATIVE TO THE IDEAL REFERENCE (MEAN OF FIVE TRIALS; ABSOLUTE AND PERCENTAGE).

Group	$\varepsilon_{\mathrm{RMS}}$ (m)	$\varepsilon_{\mathrm{RMS}}/\mathrm{R}$ (%)
G1	0.0376	8.36%
G2	0.0370	8.22%
G3	0.0387	6.45%
G4	0.0327	5.44%
G5	0.0419	4.65%
G6	0.0750	8.34%
G1&G2	0.0375	8.32%
G3&G4	0.0373	6.22%
G5&G6	0.0552	6.13%

D. Experimental Results

1) Trajectory Tracking Accuracy: Fig. 6 presents the consolidated experimental results. The left panel shows ideal and actual trajectories for all six experimental groups, while the right panel depicts the corresponding trajectory error variations. To provide a comprehensive view of tracking accuracy, Table III reports RMS trajectory errors relative to the ideal reference trajectory, in both absolute terms and as a percentage of the turning radius R. In general, all strategies can effectively track the target circular arcs, and the error remains within acceptable bounds throughout the tracking process.

Benefiting from the proposed optimization pipeline, both the front-steering (FS) and differential-steering (DS) strategies keep the normalized RMS error $(\varepsilon_{\mathrm{RMS}}/R)$ within 9% at all three turning radii, meeting engineering application requirements.

2) Energy Efficiency Analysis: Table IV summarizes the energy consumption per unit distance for each experimental group. These energy measurements were obtained using the optimized parameter sets listed in Table II, so the comparison directly reflects the energy performance of the FS and DS strategies at the same turning radius.

The experimental results show that the front steering strategy consistently consumes 12.3% less energy than the differential strategy across the three tested turning radii while maintaining comparable trajectory-tracking performance. This outcome confirms that actively regulating the front axle steering angle improves energy use in granular media. Extrapolating the measured savings to a standard $36\,\mathrm{Wh}$ battery indicates an extra travel distance of roughly $80\,\mathrm{m}$, which is meaningful for extending the robot's opera-

TABLE IV
ENERGY CONSUMPTION PER UNIT DISTANCE COMPARISON (MEAN ± STANDARD DEVIATION, 5 REPEATED TRIALS)

Group	E_{dist} (J/m)	Energy Saving vs DS
G1 (FS-0.45)	216 ± 23	+7.3%
G2 (DS-0.45)	240 ± 21	Baseline
G3 (FS-0.60)	184 ± 18	+18.9%
G4 (DS-0.60)	225 ± 20	Baseline
G5 (FS-0.90)	164 ± 18	+10.7%
G6 (DS-0.90)	176 ± 17	Baseline

tional endurance. In addition, energy consumption differences between strategies align with the simulation-predicted relative trends, indicating that despite certain simplifications in the DRFM model, it can still effectively guide actual robot system design optimization.

V. CONCLUSION

This work presents a DRFM-based optimization framework for enhancing the steering performance of wheeled mobile robots in granular environments. By coupling the Dynamic Resistive Force Model with rigid-body dynamics and employing Sobol sequence sampling, we achieve efficient optimization of steering angles and wheel velocities under trajectory constraints, as validated through comprehensive hardware experiments.

Compared to existing approaches that rely on simplified kinematic models or sensor-based feedback, our framework provides a physics-based solution that explicitly accounts for wheel-terrain interactions in particulate media, demonstrating improved energy efficiency while maintaining comparable trajectory-tracking performance for robots equipped with specialized wheel geometries.

However, the primary limitation of the current experimental setup lies in the relatively low maximum wheel rotational speed because of the high gear reduction ratio. Higher-performance motors could enable higher operational speeds while preserving trajectory fidelity.

For future work, the DRFM framework can be extended to accommodate complex terrains featuring severe topographic variations, where terrain undulations and steep gradients profoundly influence wheel-soil interactions. Furthermore, future work could leverage sensor measurements for real-time parameter identification in unknown environments, enabling integration with model predictive control (MPC) frameworks for adaptive optimization in field robotics applications.

REFERENCES

[1] M. B. Alatise and G. P. Hancke, "A review on challenges of autonomous mobile robot and sensor fusion methods," *IEEE Access*, vol. 8, pp. 39 830–39 846, 2020.

[2] R. E. Arvidson, J. F. Bell III, P. Bellutta, N. A. Cabrol, J. Catalano, J. Cohen, L. S. Crumpler, D. Des Marais, T. Estlin, W. Farrand *et al.*, "Spirit mars rover mission: Overview and selected results from the northern home plate winter haven to the side of scamander crater," *Journal of Geophysical Research: Planets*, vol. 115, no. E7, 2010.

[3] C. Samson, P. Morin, and R. Lenain, "Modeling and control of wheeled mobile robots," *Springer Handbook of Robotics*, pp. 1235–1266, 2016.

[4] B. Schäfer, A. Gibbesch, R. Krenn, and B. Rebele, "Planetary rover mobility simulation on soft and uneven terrain," *Vehicle System Dynamics*, vol. 48, no. 1, pp. 149–169, 2010.

[5] C. Li, T. Zhang, and D. I. Goldman, "A terradynamics of legged locomotion on granular media," *Science*, vol. 339, no. 6126, pp. 1408–1412, 2013.

[6] H. Askari and K. Kamrin, "Intrusion rheology in grains and other flowable materials," *Nature Materials*, vol. 15, no. 12, pp. 1274–1279, 2016.

[7] S. Agarwal, C. Senatore, T. Zhang, M. Kingsbury, K. Iagnemma, D. I. Goldman, and K. Kamrin, "Modeling of the interaction of rigid wheels with dry granular media," *Journal of Terramechanics*, vol. 85, pp. 1–14, 2019.

[8] S. Shrivastava, A. Karsai, Y. O. Aydin, R. Pettinger, W. Bluethmann, R. O. Ambrose, and D. I. Goldman, "Material remodeling and unconventional gaits facilitate locomotion of a robophysical rover over granular terrain," *Science Robotics*, vol. 5, no. 42, p. eaba3499, 2020.

[9] M. Effati and K. Skonieczny, "Systematic solution for optimally energy-efficient turning radius for wheeled skid-steer rovers," *Robotics and Autonomous Systems*, vol. 159, p. 104306, 2023.

[10] M. Cui, R. Huang, H. Liu, X. Liu, and D. Sun, "Adaptive tracking control of wheeled mobile robots with unknown longitudinal and lateral slipping parameters," *Nonlinear Dynamics*, vol. 78, pp. 1811–1826, 2014.

[11] M. Trojnacki, "Dynamics model of a four-wheeled mobile robot for control applications–a three-case study," in *Intelligent Systems' 2014: Proceedings of the 7th IEEE International Conference Intelligent Systems IS'2014, September 24-26, 2014, Warsaw, Poland, Volume 2: Tools, Architectures, Systems, Applications*. Springer, 2015, pp. 99–116.

[12] W. Li, N. Yang, J. Wang, and D. Ren, "Kinematic teleoperation of wheeled mobile robot with slippage compensation on soft terrains," *IEEE Access*, vol. 7, pp. 110 982–110 991, 2019.

[13] W. Li, J. Guo, L. Ding, J. Wang, H. Gao, and Z. Deng, "Teleoperation of wheeled mobile robot with dynamic longitudinal slippage," *IEEE Transactions on Control Systems Technology*, vol. 31, no. 1, pp. 99–113, 2022.

[14] G. Reina, L. Ojeda, A. Milella, and J. Borenstein, "Wheel slippage and sinkage detection for planetary rovers," *IEEE/ASME Transactions on Mechatronics*, vol. 11, no. 2, pp. 185–195, 2006.

[15] Z. Liang, J. Zhao, Z. Dong, Y. Wang, and Z. Ding, "Torque vectoring and rear-wheel-steering control for vehicle's uncertain slips on soft and slope terrain using sliding mode algorithm," *IEEE Transactions on Vehicular Technology*, vol. 69, no. 4, pp. 3805–3815, 2020.

[16] H.-W. Chae, J.-H. Choi, and J.-B. Song, "Robust and autonomous stereo visual-inertial navigation for non-holonomic mobile robots," *IEEE Transactions on Vehicular Technology*, vol. 69, no. 9, pp. 9613–9623, 2020.

[17] G. Ishigami, A. Miwa, K. Nagatani, and K. Yoshida, "Terramechanics-based model for steering maneuver of planetary exploration rovers on loose soil," *Journal of Field Robotics*, vol. 24, no. 3, pp. 233–250, 2007.

[18] Y. Li, L. Ding, Z. Zheng, Q. Yang, X. Zhao, and G. Liu, "A multi-mode real-time terrain parameter estimation method for wheeled motion control of mobile robots," *Mechanical Systems and Signal Processing*, vol. 104, pp. 758–775, 2018.

[19] J. Guo, W. Li, L. Ding, H. Gao, T. Guo, B. Huang, and Z. Deng, "Linear expressions of drawbar pull and driving torque for grouser-wheeled planetary rovers without terrain mechanical parameters," *IEEE Robotics and Automation Letters*, vol. 6, no. 4, pp. 8197–8204, 2021.

[20] S. Agarwal, D. I. Goldman, and K. Kamrin, "Mechanistic framework for reduced-order models in soft materials: Application to three-dimensional granular intrusion," *Proceedings of the National Academy of Sciences*, vol. 120, no. 4, p. e2214017120, 2023.

[21] R. D. Maladen, Y. Ding, C. Li, and D. I. Goldman, "Undulatory swimming in sand: subsurface locomotion of the sandfish lizard," *Science*, vol. 325, no. 5938, pp. 314–318, 2009.

[22] T. Zhang and D. I. Goldman, "The effectiveness of resistive force theory in granular locomotion," *Physics of Fluids*, vol. 26, no. 10, 2014.

[23] L. Huang, J. Zhu, Y. Yuan, and Y. Yin, "A dynamic resistive force model for designing mobile robot in granular media," *IEEE Robotics and Automation Letters*, vol. 7, no. 2, pp. 5357–5364, 2022.